University of Dundee

Stability of chemical reaction fronts in solids

Morozov, A.; Poluektov, Michael; Freidin, A. B.; Figiel, Łukasz; Müller, W. H.

Download date: 29. Jan. 2024

Full length article

Stability of chemical reaction fronts in solids: Analytical and numerical approaches

A. Morozov [a], M. Poluektov [b,d,*], A.B. Freidin [c], Ł. Figiel [b,e], W.H. Müller [a]

[a] *Berlin Institute of Technology, Institute of Mechanics, Einsteinufer 5, 10587 Berlin, Germany*
[b] *IINM, WMG, University of Warwick, Coventry CV4 7AL, UK*
[c] *Institute for Problems in Mechanical Engineering of the Russian Academy of Sciences, 61 Bolshoy pr. V.O., St. Petersburg 199178, Russia*
[d] *Department of Mathematical Sciences and Computational Physics, School of Science and Engineering, University of Dundee, Dundee DD1 4HN, UK*
[e] *Warwick Centre for Predictive Modelling, University of Warwick, Coventry CV4 7AL, UK*

ARTICLE INFO

ABSTRACT

Localized chemical reactions in deformable solids are considered. A chemical transformation is accompanied by the transformation strain and emerging mechanical stresses, which affect the kinetics of the chemical reaction front to the reaction arrest. A chemo-mechanical coupling via the chemical affinity tensor is used, in which the stresses affect the reaction rate. The emphasis is made on the stability of the propagating reaction front in the vicinity of the blocked state. There are two major novel contributions. First, it is shown that for a planar reaction front, the diffusion of the gaseous-type reactant does not influence the stability of the reaction front – the stability is governed only by the mechanical properties of solid reactants and stresses induced by the transformation strain and the external loading, which corresponds to the mathematically analogous phase transition problem. Second, the comparison of two computational approaches to model the reaction front propagation is performed – the standard finite-element method with a remeshing technique to resolve the moving interface is compared to the cut-finite-element-based approach, which allows the interface to cut through the elements and to move independently of the finite-element mesh. For stability problems considered in the present paper, the previously-developed implementation of the cut-element approach has been extended with the additional post-processing procedure that obtains more accurate stresses and strains, relying on the fact that the structured grid is used in the implementation. The approaches are compared using a range of chemo-mechanical problems with stable and unstable reaction fronts.

1. Introduction

Problems with propagating interfaces are encountered in various solid mechanics problems, such as stress-induced phase transitions and chemo-mechanics. Propagating interfaces in phase transition problems (e.g., martensitic transformation) have been studied analytically and numerically during last decades within the framework of mechanics of configurational forces (Abeyaratne and Knowles, 1991; Liu, 1992; Socrate and Parks, 1993; Müller and Gross, 1999; Gurtin, 2000; Gross et al., 2002; Abeyaratne and Knowles, 2006; Berezovski et al., 2008; Maugin, 2010). Propagation of chemical reaction fronts in solids presents a particular interest to researchers due to interdisciplinarity and relevance to modern industry. Such problems include formation of oxide layers on polycrystalline Si parts of micro-electro-mechanical systems (MEMS) and the subsequent fracture, impacting the lifetime of MEMS (Muhlstein et al., 2002a,b; Muhlstein and Ritchie, 2003); growth

of the intermetallic compound phases in solder-based joints (Kim and Tu, 1996; Schaefer et al., 1998; Böhme et al., 2009; Anders et al., 2012; Schuß et al., 2018; Arafat et al., 2020; Wang et al., 2020; Morozov et al., 2020); lithiation of Si in Li-ion batteries (McDowell et al., 2013; Cui et al., 2013; Poluektov et al., 2018; Wu et al., 2018; Abali, 2020; Wang et al., 2021; Viana et al., 2023); and paint degradation under metal soap formation in historical paintings (Eumelen et al., 2019, 2023). Experimental evidence shows that in such problems, mechanical stresses affect the reaction front kinetics — the stresses can accelerate, retard, or even block the propagation of chemical reaction fronts (Marcus and Sheng, 1982; Kao et al., 1988; Mihalyi et al., 1999; Heidemeyer et al., 2000; Büttner and Zacharias, 2006; Liu et al., 2013; van Havenbergh et al., 2016). Moreover, the stresses also influence the stability of the propagating fronts (Suo et al., 1992; Barvosa-Carter et al., 1998; Ortiz et al., 1999; Phan et al., 2001; Barvosa-Carter et al.,

---

2004; Ahmad and Viswanathan, 2017), which is relevant to the solid electrolyte interphase (SEI) formation in Li-ion batteries (Natsiavas et al., 2016; Hüter et al., 2017), where the formation and growth of a dendrite, which can be considered as an instability, can induce delamination or cause an inner short circuit (Monroe and Newman, 2005; Doux et al., 2020; Qin et al., 2020; Gao and Lu, 2022).

In the case of quasi-static stress-induced phase transitions, the configurational force driving the interface propagation is given by the jump of the normal component of the Eshelby stress tensor (Šilhavý, 1997; Gurtin, 2000; Abeyaratne and Knowles, 2006; Maugin, 2010). Zero configurational force is a necessary criterion for the phase equilibrium. However, the interface may be stable or unstable (Grinfeld, 1991). In the case of localized chemical reactions, zero configurational force corresponds to the chemical equilibrium, at which the reaction front propagation is blocked. The chemical reaction front may also be stable or unstable (Morozov et al., 2019a, 2023), and the front may be directed to unstable configurations by the supply of the diffusive reactant. Therefore, the question regarding the stability of the reaction fronts arises naturally. Not only interfaces at equilibrium can be stable or unstable, but also propagating ones — a perturbation of the propagating interface can decay or grow, which corresponds to the stable and the unstable scenarios, respectively.

In Eremeev et al. (2003) and Yeremeyev et al. (2007), it has been shown that in the case of isotropic phases, in a sphere undergoing phase transition, a new phase nucleation may start either in the center or at the outer surface of the sphere, depending on the energy expression. One of these cases is unstable even if it satisfies the phase equilibrium conditions. In a similar case of a sphere undergoing a localized chemical reaction, the supply of the diffusive constituent at the outer surface determines where the nucleation of the new phase starts. Therefore, the new phase might grow at the outer surface of a sphere, despite this configuration being potentially unstable.

From a mathematical point of view, a general problem of coupled chemo-mechanics with localized chemical reactions represents a system of PDEs defined on a domain with time-dependent interfaces. There is a large variety of numerical approaches that can handle problems with propagating interfaces. All of them can be divided into two groups considering either a smooth or a sharp representation of the interface. A typical example of the smooth-interface approach is the phase-field method, e.g., Svendsen et al. (2018), Weinberg et al. (2018) in application to chemo-mechanics and Schneider et al. (2017, 2018) in application to phase transitions. The sharp-interface methods can be divided into a number of subcategories by the type of discretization of the equations. One example of such method is the boundary integral method, e.g., Su and Voorhees (1996a,b), Jou et al. (1997) in application to chemo-mechanics. A more widespread approach is the finite-element method, application of which to chemo-mechanics is the main focus of the present paper.

All sharp-interface finite-element-based methods can be divided into three subcategories. The first subcategory covers the case of the interface coinciding with the element edges/faces in 2D/3D and the geometry being completely remeshed each time the interface propagates, e.g., Freidin et al. (2016, 2022) in application to chemo-mechanics. The second subcategory also relies on the interface coinciding with the element edges/faces; however, the mesh in only distorted as the interface moves, i.e., the nodes are moved, without changing the number or the connectivity of the nodes, e.g., Morozov et al. (2018) in application to chemo-mechanics, where such approach has been implemented using the isogeometric method.

The third subcategory contains approaches where the interface cuts through the finite-element mesh in an arbitrary way and moves independently of the mesh, which is unchanged from one time increment to another. A typical example of such approach is the combination of the extended finite-element method (XFEM) to solve the PDEs and the level-set method to move the interface, e.g., Zhao et al. (2013a,b) in application to the phase transitions and Duddu et al. (2011), Zhao

et al. (2015) in application to chemo-mechanics. Another example of such approach is the CutFEM method, which has been originally formulated for linear problems (Hansbo and Hansbo, 2002; Burman and Hansbo, 2012) and subsequently has been adapted specifically to linear elasticity (Hansbo et al., 2017; Burman et al., 2018, 2019a,b). Recently, the CutFEM method has been adapted to problems of chemo-mechanics (Poluektov and Figiel, 2019), where the numerical method has been formulated for the general finite-strain chemo-mechanical setting, i.e., involving non-linear PDEs. The CutFEM method relies on two main features — the enforcement of the interface conditions weakly using the Nitsche method (Nitsche, 1971), which allows solving the discretized PDEs with the interface cutting through the elements, and the introduction of an inter-element stabilization, which addresses the ill-conditionality of the discrete problem related to the interface partitioning the elements into highly unequal spatial fractions.

The present paper continues the study of the stability of chemical reaction fronts, started in Morozov (2021) and Morozov et al. (2023), where the kinetics of the interface is governed by the chemical affinity tensor, developed in Freidin (2013) and Freidin et al. (2014). A perturbed kinetic equation in the vicinity of the equilibrium position of the chemical reaction front is considered, similarly to the case of phase transitions (Yeremeyev et al., 2007). It should be noted that the kinetic stability analysis performs not only an energy-based verification of the stability and states the fact of the stability loss, but also gives hints on modes of instability formation and the tendencies of further kinetics of the perturbations. Analytical investigation of the interface stability based on the perturbed kinetic equation is relatively complex, even for simple geometries. Non-trivial geometries require a numerical procedure to capture the aforementioned stability behavior. Therefore, the aim of the present paper is twofold: (a) to perform the linear stability analysis for a planar chemical reaction front, (b) to compare two computational approaches for modeling chemical reaction front propagation — the standard finite-element method with a remeshing technique and the CutFEM-based approach.

2. Coupled chemo-mechanics with localized chemical reaction

A chemical reaction between the solid and the diffusive constituents is considered. The reaction is localized at the chemical reaction front — a sharp interface separating the chemically transformed and the untransformed phases. The diffusive constituent is supplied from the external environment and diffuses to the reaction front through the transformed phase, as illustrated in Fig. 1. A typical chemical reaction of this type is

$$n_- B_- + n_* B_* \longrightarrow n_+ B_+, \tag{1}$$

where B_-, B_*, B_+ stand for the untransformed phase, the diffusive constituent, the chemically transformed phase, respectively; n_-, n_*, n_+ are the corresponding stoichiometric coefficients. Since the reaction is localized, its evolution in time consists in propagation of the chemical reaction front. From the mass balance, it follows that the normal component of the reaction front velocity, denoted as $V_{\Gamma_*}^{\mathrm{ch}}$, is related to chemical reaction rate ω at the oriented surface element of the reaction front (defined as the amount of substance produced by the reaction per unit area and per unit of time) as

$$V_{\Gamma_*}^{\mathrm{ch}} = \frac{n_- M_-}{\rho_-} \omega, \tag{2}$$

where M_- and ρ_- are the molar mass and the density of the untransformed material, respectively (Freidin, 2013; Freidin and Vilchevskaya, 2020).

The scope of the present paper is limited to consideration of a single reaction front and linear elastic behavior of the materials, as the latter allows studying analytically the front stability. It is also possible to consider more complex constitutive behavior (e.g., including viscosity), but the analytical solutions become much more cumbersome
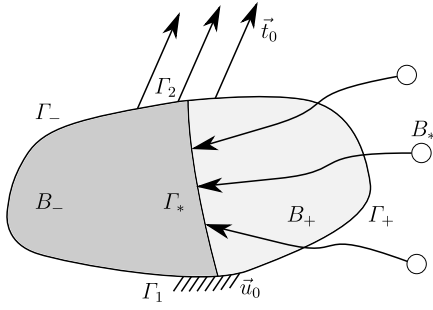
Fig. 1. A schematic representation of a localized chemical reaction in a deformable solid.

or even impossible. Moreover, chemical processes can involve multiple diffusive species, and the reactions can occur at multiple chemical reaction fronts, at each of which, the solid component reacts with a single diffusive constituent. An example of the latter is the formation of intermetallic compounds in lead-free solder alloys, which has been modeled in Morozov et al. (2019b) using the same framework as used in the present paper, however, without addressing the question of stability.

In the linear-elastic case, the general chemo-mechanical problem with the localized reaction can be formulated as follows. Non-stationary chemical reaction front Γ_* splits the domain of the solid body into Ω_+ and Ω_-, which are the domains occupied by the transformed and the untransformed phases, respectively. Material deformation is governed by the linear momentum balance equation,

$$\nabla \cdot \sigma_\pm = \vec{0} \qquad \text{in } \Omega_\pm, \tag{3}$$

where $\sigma_\pm$ and $\varepsilon_\pm$ denote the stress and the infinitesimal linear strain tensors, respectively, in the transformed and the untransformed phases, related by the following constitutive laws:

$$\sigma_+ = {}^4C_+ : \left(\varepsilon_+ - \varepsilon^{\text{ch}}\right) \qquad \text{in } \Omega_+,$$
$$\sigma_- = {}^4C_- : \varepsilon_- \qquad \text{in } \Omega_-,$$

where ${}^4C_\pm$ are the stiffness tensors of the materials. Subscripts "+" and "−" denote the variables corresponding to materials B_+ and B_-, respectively. Subscripts "$\pm$" and "$\mp$" are used to indicate that the considered equation consists of two equations, where the first is written with the upper signs and the second is written with the lower signs. When function's arguments contain a variable with subscript "$\pm$", it denotes that the function depends both on the variable with subscript "+" and the variable with subscript "−". A chemical transformation (e.g., volumetric expansion) is represented in the model as transformation strain ε^{ch}. The displacement and the traction continuity conditions at the chemical reaction front are enforced:

$$[\![\vec{u}]\!] = \vec{0} \quad \text{and} \quad [\![\sigma]\!] \cdot \vec{N}_* = \vec{0} \qquad \text{on } \Gamma_*, \tag{4}$$

where $\vec{N}_*$ is the normal to the reaction front, defined as the outer normal to the domain occupied by the transformed material. Brackets $[\![\cdot]\!]$ denote the jump of a quantity across the interface. The displacement and/or the traction boundary conditions are prescribed at the outer surface of the body.

The following assumptions regarding the diffusion are made: (A) the diffusion process is much faster than the chemical reaction rate, and the transient diffusion regime can be neglected; (B) the diffusion takes place only inside the transformed material, and the diffusive reactant approaching reaction front Γ_* is entirely consumed at the reaction front; (C) the classical Fickian diffusion is considered, in which the mechanical stresses do not affect the diffusion kinetics in the bulk.

Assumption (A) implies that in the considered problems, the front propagation is controlled by the chemical reaction rate, i.e., the processes at the front, rather than by the diffusive transport taking place

over a long range, which has been observed experimentally during the initial stages of Si lithiation (Liu et al., 2011). This assumption also leads to the stationary diffusion formulation, which has been previously used for modeling of the front kinetics based on the chemical affinity tensor in, e.g., Freidin et al. (2014), Poluektov et al. (2018). It is also worth mentioning that in Zhao et al. (2012), Jia and Li (2015), localized Si lithiation has been modeled and the diffusion has been assumed to be fast enough to allow for a uniform distribution of lithium, which is a stronger assumption than the stationarity of the diffusion.

Assumption (B) is also motivated experimentally — for example, for the localized reaction between Li and Si, there is a direct experimental evidence that the diffusive species are confined to the transformed (lithiated) material (Liu et al., 2012). In the latter work, it has been shown experimentally that during lithiation of crystalline Si, the thickness of the reaction zone is around 2 nm. If micrometer-size samples are considered, then such reaction front can be modeled as being infinitely thin. Similar infinitely-thin reaction zones are observed during formation of intermetallic compounds (Morozov et al., 2020). These observations also motivate the sharp interface model of the reaction front.

Finally, since the front velocity is controlled by the chemical reaction rate, the influence of the mechanical stresses on the supply of the diffusive reactant can be considered to have a minor effect on the front velocity, compared to the effect of the stresses on the consumption rate at the front (i.e., the reaction rate), justifying assumption (C). It should be noted that there is a wide range of models, in which the stresses do affect the diffusion, e.g., Cui et al. (2012), Brassart and Suo (2012, 2013), Levitas and Attariani (2014).

Based on assumptions (A)–(C), the following mass balance equation for the diffusive constituent is considered:

$$\Delta c = 0 \qquad \text{in } \Omega_+, \tag{5}$$

where c is the molar concentration of the diffusive reactant and Δ is the Laplace operator, with the following boundary condition at the reaction front:

$$D\vec{N}_* \cdot \nabla c + n_* \omega = 0 \qquad \text{on } \Gamma_*, \tag{6}$$

where D is the diffusion coefficient of the diffusive reactant through the transformed material. At the reactant supply surface Γ_a, which is a part of the external boundary of the body, the mixed boundary condition is prescribed:

$$D\vec{N} \cdot \nabla c - \alpha \left(c_* - c\right) = 0 \qquad \text{on } \Gamma_a, \tag{7}$$

where α is the surface mass transfer coefficient, c_* is the solubility of the diffusive reactant in the transformed phase, and $\vec{N}$ is the normal to the outer boundary of the body.

To model the kinetics of the reaction front, the theory based on the chemical affinity tensor concept (Freidin, 2013; Freidin et al., 2014; Freidin and Vilchevskaya, 2020) is used. It should be noted that the theory is general and covers arbitrary rheology and large deformations; however, in the present paper, the linear elastic version is used. According to this theory, the quantity that is referred to as the chemical affinity tensor is the driving force for the localized chemical reaction. The normal component of the chemical affinity tensor in the quasi-static linear-elastic case is written as

$$A_{NN} = \frac{n_- M_-}{\rho_-} \chi \left(\sigma_\pm, \varepsilon_\pm, T\right) + n_* RT \ln \frac{c}{c_*}, \tag{8}$$

where R is the universal gas constant, T is the absolute temperature, and

$$\chi \left(\sigma_\pm, \varepsilon_\pm, T\right) = \gamma (T) - \zeta \left(\sigma_\pm, \varepsilon_\pm\right) =$$
$$= \gamma (T) + \frac{1}{2}\sigma_- : \varepsilon_- - \frac{1}{2}\sigma_+ : \left(\varepsilon_+ - \varepsilon^{\text{ch}}\right) + \sigma_\pm : [\![\varepsilon]\!], \tag{9}$$

where $\zeta\left(\sigma_\pm, \varepsilon_\pm\right)$ characterizes the influence of the stress–strain states on the reaction front kinetics and $\gamma(T)$ denotes the temperature-dependent chemical energy of the reaction. The expression for the chemical affinity tensor has been obtained from the balance laws and the dissipation inequality.

The kinetics of the reaction is related to the driving force via the constitutive law. In the present paper, the form of the kinetic equation from the classical physical chemistry (Prigogine and Defay, 1954; Glansdorff and Prigogine, 1971) is used:

$$\omega = k_* c \left(1 - \exp\left(-\frac{A_{NN}}{RT}\right)\right), \tag{10}$$

where k_* is a reaction rate constant. The details can be found in, e.g., Freidin and Vilchevskaya (2020). If $A_{NN} = 0$ for the reaction front surface element with normal $\vec{N}_*$, then such surface element is at the chemical equilibrium. In this case, the reaction rate and, therefore, the front propagation velocity are zero. If $A_{NN} = 0$ is fulfilled at each point of the reaction front, then such configuration is an equilibrium configuration.

It should be noted that from the mathematical point of view, the considered chemical reaction front kinetics is similar to the problem of stress-induced phase transitions, e.g., Abeyaratne and Knowles (1991, 2006), Berezovski and Maugin (2005), where the following form of the expression for the normal component of the velocity is used:

$$V_{\Gamma_*}^{\mathrm{ph}} = k_{\mathrm{ph}} \chi\left(\sigma_\pm, \varepsilon_\pm, T\right), \tag{11}$$

where k_{ph} is a kinetic coefficient. In this case, there is no diffusive constituent and parameter $\gamma(T)$ is no longer a chemical reaction energy, but a difference in the free energy volume densities of the solid constituents in the stress-free states. This mathematical similarity between the chemo-mechanics and the phase transitions is used later in the paper to study the influence of the diffusion on the stability of the propagating interface.

3. Linear stability analysis of the reaction front

A given reaction front can be stable or unstable. The latter implies that a perturbation of the front decays over time, while the former implies the opposite. The considered reaction front can be either propagating or at the equilibrium. The approach for analyzing the stability of the chemical reaction fronts has been developed in Morozov (2021), Morozov et al. (2023) based on a similar methodology developed earlier for the stress-induced phase transition problems (Eremeev et al., 2003; Yeremeyev et al., 2007).

The approach can be summarized as follows. Some configuration of the reaction front is considered, at which $\vec{R}_*^0$ denotes the position of the points of the front and $\vec{N}_*^0$ denotes the normal to the front. At this state, the solutions of PDEs (3) and (5) are displacements $\vec{u}_\pm^0$ and concentration c^0. The stresses and strains emerging in the body are denoted as $\sigma_\pm^0$ and $\varepsilon_\pm^0$, respectively. From this point onwards, superscript "0" refers to variables that belong to the solution corresponding to the unperturbed configuration.

The position of the points of the front in the perturbed state is given by

$$\vec{R}_* = \vec{R}_*^0 + \eta \vec{N}_*^0, \tag{12}$$

where η is the amplitude of the perturbation, as illustrated in Fig. 2. The perturbation of the front necessary leads to the perturbation of the solutions of the PDEs:

$$\vec{u}_\pm = \vec{u}_\pm^0 + \vec{w}_\pm, \tag{13}$$

$$c = c^0 + s, \tag{14}$$

where $\vec{w}_\pm$ and s are the perturbations of the displacements and the concentration, respectively. The key idea of the approach is to rewrite the kinetic equation for the front propagation with respect to η and
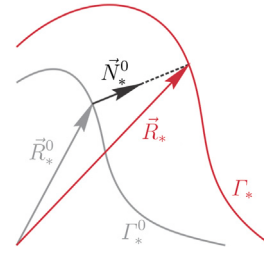

Fig. 2. A schematic representation of the perturbed and the unperturbed reaction fronts (Γ_* and Γ_*^0, respectively).

to verify whether it increases or decreases, which corresponds to the unstable or the stable configurations, respectively.

The perturbations above lead to two boundary value problems (BVPs) — the first is for the considered configuration of the reaction front (with solutions $\vec{u}_\pm^0$ and c^0), the second is for the case when the reaction front is perturbed (with solutions $\vec{w}_\pm$ and s). To find the solution of the perturbed BVP, expressions (13) and (14) must be substituted into PDEs (3) and (5). However, the PDEs are now defined on a domain with a perturbed interface. To solve the equations, it is convenient to replace the domain by one with the unperturbed interface. This is done by linearizing interface conditions (4) and (6) with respect to perturbations η, $\vec{w}_\pm$, s and projecting the interface conditions onto the unperturbed geometry.

It is implied that in this procedure, terms $O\left(\eta^2\right)$ are neglected. Moreover, perturbation η is a function of both space and time and the linearization is done only with respect to the time dependency. This means that η and $\nabla\eta$ are of the same order, while $\eta\nabla\eta$ and η^2 are one order higher. The same is valid for $\vec{w}_\pm$, for example, η, $\vec{w}_\pm$, $\nabla\vec{w}_\pm$ are of the same order, while $\eta\nabla\vec{w}_\pm$ is one order higher. This will be more evident later when the solution is sought in a series form for the flat reaction front and η, $\vec{w}_\pm$, s are decomposed into the spatial and the temporal parts.

For the linear momentum balance equation, the linearization and the projection of the interface conditions onto the unperturbed geometry was done in Eremeev et al. (2003) and Yeremeyev et al. (2007) and the detailed derivation is also given in Morozov et al. (2023). This gives the following BVP for the mechanical part of the problem:

$$\nabla \cdot \sigma_\pm\left(\vec{w}_\pm\right) = \vec{0} \qquad \text{in } \Omega_\pm, \tag{15}$$

$$\sigma_\pm\left(\vec{w}_\pm\right) = {}^4 C_\pm : \nabla\vec{w}_\pm,$$

$$[\![\vec{w}]\!] = -\eta\vec{N}_*^0 \cdot [\![\nabla\vec{u}^0]\!] \qquad \text{and}$$

$$\vec{N}_*^0 \cdot [\![\sigma\left(\vec{w}\right)]\!] = \tilde{\nabla}\eta \cdot [\![\sigma^0]\!] - \eta\vec{N}_*^0\vec{N}_*^0 : [\![\nabla\sigma^0]\!] \qquad \text{on } \Gamma_*,$$

where $\tilde{\nabla}$ is the "flat" Nabla operator, containing only the derivatives along the tangential to the interface vectors. For the diffusion equation, the linearization and the projection of the interface conditions onto the unperturbed geometry was done in Morozov et al. (2023), which gives the following BVP for the diffusion:

$$\Delta s = 0 \qquad \text{in } \Omega_+, \tag{16}$$

$$D\vec{N}_*^0 \cdot \nabla s + D\eta\vec{N}_*^0\vec{N}_*^0 : \nabla\nabla c^0 - D\tilde{\nabla}\eta \cdot \nabla c^0 + n_*\delta\omega\left(\eta, \vec{w}_\pm, s\right) = 0 \quad \text{on } \Gamma_*,$$

where $\delta\omega\left(\eta, \vec{w}_\pm, s\right)$ is the perturbation of the reaction rate, which is obtained by the linearization and the projection of expression (10) onto the unperturbed geometry. It is given by

$$\delta\omega\left(\eta, \vec{w}_\pm, s\right) = k_* c^0 \frac{1}{RT}\frac{n_- M_-}{\rho_-}\delta\chi\left(\eta, \vec{w}_\pm\right) +$$

$$+ \left(k_* n_* + \frac{1 - n_*}{c^0}\omega^0\right)\left(s + \eta\vec{N}_*^0 \cdot \nabla c^0\right), \tag{17}$$

where ω^0 is the reaction rate at the unperturbed state and $\delta\chi\left(\eta, \vec{w}_\pm\right)$ is the perturbation of $\chi\left(\sigma_\pm, \varepsilon_\pm, T\right)$. The latter is obtained by the linearization and the projection of expression (9) onto the unperturbed

geometry. It should be noted that χ was introduced in Eq. (9) as a function of $\sigma_\pm$, $\varepsilon_\pm$, T that are taken at the reaction front, while here, it is implied that for the perturbed problem, fields $\sigma_\pm^0$ and $\varepsilon_\pm^0$ are fixed, hence, $\delta\chi$ becomes a function of η and $\vec{w}_\pm$.

The linearization and the projection onto the unperturbed geometry of the expression for χ was performed and specified for the equilibrium two-phase spherically-symmetric deformations in Eremeev et al. (2003), Yeremeyev et al. (2007) within the context of the phase transition problems. It was then generalized for the case of a propagating chemical reaction front without any symmetry restrictions in Morozov et al. (2023). This expression contained the stresses and strains only at one side of the interface and the normal; it was derived and used for the analytical studies. However, a different way of writing $\delta\chi$ is used in the present paper. To simplify the presentation of the approach and since the resulting system of equations is solved numerically (the details are given below), expression (9) is directly linearized and projected (Appendix), which results in

$$\delta\chi\left(\eta, \vec{w}_\pm\right) = \left[\!\left[\nabla\vec{u}^0\right]\!\right] : \left(\sigma_+\left(\vec{w}_+\right) + \eta\vec{N}_*^0 \cdot \nabla\sigma_+^0\right) - $$
$$- \left[\!\left[\sigma^0\right]\!\right] : \left(\nabla\vec{w}_- + \eta\vec{N}_*^0 \cdot \nabla\nabla\vec{u}_-^0\right). \qquad (18)$$

BVPs (15) and (16) should be solved to find $\vec{w}_\pm$ and s as functions of η and substituted into kinetic equation (2), from which perturbation η as a function of time should be found. Its growth or decay indicates instability or stability, respectively, of the reaction front.

4. Stability of the planar reaction front

A chemical reaction in a layer of thickness H is considered, as illustrated in Fig. 3. Initial and transformed materials are considered to be isotropic and the plane strain formulation is used. It is assumed that the parameters and the loading are such that there exists an equilibrium position $y = h$, $h \in (0, H)$ of a planar reaction front inside the body. The problem under consideration is to determine whether this equilibrium configuration is stable or unstable.

The diffusive constituent is supplied through the bottom boundary. Thus, the following boundary conditions for PDEs (3) and (5) are used:

$$\vec{u}_+ = \vec{0} \qquad \text{at } y = 0, \qquad (19)$$

$$\vec{u}_- = u_0\vec{e}_y \qquad \text{at } y = H, \qquad (20)$$

$$\vec{u}_\pm \cdot \vec{e}_x = 0 \quad \text{and} \quad \sigma_\pm : \vec{e}_x\vec{e}_y = 0 \qquad \text{at } x = 0 \text{ and } x = L, \qquad (21)$$

$$D\vec{N} \cdot \nabla c + \alpha\left(c - c_*\right) = 0 \qquad \text{at } y = 0, \qquad (22)$$

$$\vec{N} \cdot \nabla c = 0 \qquad \text{at } x = 0 \text{ and } x = L, \qquad (23)$$

where L is the width of the considered domain. A planar isotropic transformation strain is considered:

$$\varepsilon^{\text{ch}} = \frac{\theta}{2}\left(I - \vec{e}_z\vec{e}_z\right), \qquad (24)$$

where $\vec{e}_z$ is the out-of-plane unit vector and I is the unit tensor, θ is the intrinsic volume change of the untransformed phase to the chemically transformed phase. As the solid skeleton approach is adopted in the present paper (Freidin and Vilchevskaya, 2020), θ is treated as a parameter of the chemical reaction. For simplicity, isotropic elasticity will be considered from this point onwards, with $\lambda_\pm$ and $\mu_\pm$ standing for the Lamé parameters corresponding to domains $\Omega_\pm$.

The choice of boundary conditions in terms of displacements is motivated, in particular, by the fact that in the case of solid–solid phase transitions, the two-phase state may be *a priori* unstable if the external loading (traction) is prescribed at the boundary, as discussed in, e.g., Yeremeyev et al. (2007), Freidin et al. (2021). Since, in the present paper, the phase transition and the chemo-mechanical problems are compared, the prescribed displacements at the boundary are imposed. In addition, when the material parameters are fixed, the variation of u_0 changes the equilibrium position of the front within the domain, which is convenient for further investigations.
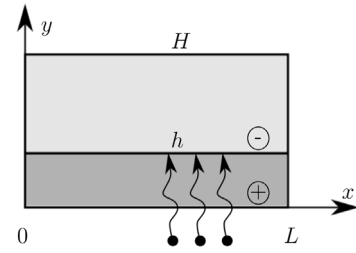

Fig. 3. A schematic representation of the planar chemical reaction front.

Following the procedure outlined in Section 3, the unperturbed BVP is solved first to obtain $\vec{u}_\pm^0$ and c^0, and, hence, to find $\sigma_\pm^0$ and $\varepsilon_\pm^0$. For the planar problem at the equilibrium configuration considered here, the closed form expressions for these quantities can be easily obtained. It should be noted that in this case, the displacement field is piecewise-linear and $c^0 = c_*$. Consequently, ∇c^0, $\nabla\sigma_\pm^0$, $\nabla\nabla\vec{u}_\pm^0$, χ^0, ω^0 are equal to zero.

To solve the perturbed BVP, the boundary conditions must be written by substituting Eqs. (13)–(14) into (19)–(23), resulting in

$$\vec{w}_\pm = \vec{0} \qquad \text{at } y = 0 \text{ and } y = H$$

$$\vec{w}_\pm \cdot \vec{e}_x = 0 \quad \text{and} \quad \sigma_\pm\left(\vec{w}_\pm\right) : \vec{e}_x\vec{e}_y = 0, \qquad \text{at } x = 0 \text{ and } x = L,$$

$$D\vec{N} \cdot \nabla s + \alpha s = 0 \qquad \text{at } y = 0,$$

$$\vec{N} \cdot \nabla s = 0 \qquad \text{at } x = 0 \text{ and } x = L.$$

For the planar reaction front, $\vec{N}_*^0 = \vec{e}_y$ and $\eta = \eta(x, t)$. It is useful to rewrite the perturbation of the solution in the component form:

$$\vec{w}_\pm = w_x^\pm(x, y, t)\vec{e}_x + w_y^\pm(x, y, t)\vec{e}_y, \qquad (25)$$

$$s = s(x, y, t). \qquad (26)$$

The solution of the perturbed BVPs (15) and (16) results in the dependency of displacements $\vec{w}_\pm$ and concentration s (and, therefore, the reaction front velocity) on amplitude η of the perturbation of the front. For the case of the planar front, these dependencies can be obtained semi-analytically in a series form (the coefficients are still found computationally). To satisfy the boundary conditions at $x = 0$ and $x = L$, the solution is sought as series

$$w_x^\pm(x, y, t) = \sum_{n=1}^\infty U_n^\pm(y, t)\sin\left(k_nx\right), \quad w_y^\pm(x, y, t) = \sum_{n=1}^\infty V_n^\pm(y, t)\cos\left(k_nx\right),$$

$$\eta(x, t) = \sum_{n=1}^\infty \xi_n(t)\cos\left(k_nx\right), \quad s(x, y, t) = \sum_{n=1}^\infty S_n(y, t)\cos\left(k_nx\right), \quad k_n = \frac{n\pi}{L}.$$

First, the perturbed displacements can be found. One can show that functions $U_n^\pm(y, t)$ and $V_n^\pm(y, t)$ that satisfy Eq. (15) are

$$U_n^\pm(y, t) = A_n^\pm(t)\exp\left(k_ny\right) + $$
$$+ B_n^\pm(t)\,y\exp\left(k_ny\right) + C_n^\pm(t)\exp\left(-k_ny\right) + D_n^\pm(t)\,y\exp\left(-k_ny\right),$$

$$V_n^\pm(y, t) = \left(-A_n^\pm(t) + B_n^\pm(t)\frac{\lambda_\pm + 3\mu_\pm}{\lambda_\pm + \mu_\pm}\frac{1}{k_n}\right)\exp\left(k_ny\right) - $$

$$- B_n^\pm(t)\,y\exp\left(k_ny\right) + \left(C_n^\pm(t) + D_n^\pm(t)\frac{\lambda_\pm + 3\mu_\pm}{\lambda_\pm + \mu_\pm}\frac{1}{k_n}\right)\exp\left(-k_ny\right) + $$

$$+ D_n^\pm(t)\,y\exp\left(-k_ny\right).$$

Functions $A_n^\pm$, $B_n^\pm$, $C_n^\pm$, $D_n^\pm$ are then found from the boundary and the interface conditions of BVP (15). The time dependency of these functions comes from the dependency of the interface conditions on $\eta(x, t)$. One should note that, due to the boundary and the interface conditions, each function $A_n^\pm$, $B_n^\pm$, $C_n^\pm$, $D_n^\pm$ is proportional to $\xi_n(t)$, e.g., $A_n^\pm(t) = a_n^\pm\xi_n(t)$, where $a_n^\pm$ are constants. This allows expressing $\delta\chi$ as a function of ξ_n:

$$\delta\chi(x, t) = \sum_{n=1}^\infty L_n^{\text{ph}}\xi_n(t)\cos\left(k_nx\right), \qquad (27)$$

where L_n^{ph} is a constant.

Next, the perturbed concentration can be obtained. One can show that function $S_n(y,t)$ that satisfies Eq. (16) is

$$S_n(y,t) = E_n(t)\exp(k_n y) + F_n(t)\exp(-k_n y). \tag{28}$$

Functions E_n, F_n are found from the boundary conditions. Furthermore, due to the boundary conditions, each function E_n, F_n is proportional to $L_n^{\text{ph}}\xi_n(t)$. More specifically,

$$E_n(t) = L_n^{\text{ph}}\xi_n(t)\,\frac{-\psi}{\phi_n}, \qquad F_n(t) = L_n^{\text{ph}}\xi_n(t)\,\frac{-\psi}{\phi_n}\frac{Dk_n-\alpha}{Dk_n+\alpha}, \tag{29}$$

where the following quantities are introduced:

$$\phi_n = \left(Dk_n + n_*^2 k_*\right)\exp(k_n h) - \left(Dk_n - n_*^2 k_*\right)\frac{Dk_n-\alpha}{Dk_n+\alpha}\exp(-k_n h),$$

$$\psi = n_* k_* c_* \frac{1}{RT}\frac{n_- M_-}{\rho_-}.$$

Linearization of the normal front velocity (2), where $O\left(\eta^2\right)$ terms are neglected, gives

$$V_{\Gamma_*}^{\text{ch}} = \vec{N}_* \cdot \frac{\mathrm{d}}{\mathrm{d}t}\vec{R}_* = \frac{\mathrm{d}\eta}{\mathrm{d}t}. \tag{30}$$

By using kinetic equation Eq. (2), substituting (27) into (17), then substituting (29) into (28) and into the expression for $s(x,y,t)$ and into (17), the following equation for the evolution of the perturbation is obtained:

$$\frac{n_*}{\psi}\frac{\rho_-}{n_- M_-}\frac{\mathrm{d}\xi_n}{\mathrm{d}t} = L_n^{\text{ch}}\xi_n, \tag{31}$$

where

$$L_n^{\text{ch}} = L_n^{\text{ph}}\left(1 - \frac{n_*^2 k_* \exp(k_n h) + n_*^2 k_*\frac{Dk_n-\alpha}{Dk_n+\alpha}\exp(-k_n h)}{\phi_n}\right). \tag{32}$$

The specific form of the obtained expression for L_n^{ch} is useful in the following way. It is easy to show that the expression in brackets in (32) is always positive. Indeed, Eq. (32) can be rewritten as

$$L_n^{\text{ch}} = L_n^{\text{ph}}\frac{2Dk_n\left(Dk_n \sinh(k_n h) + \alpha \cosh(k_n h)\right)}{\phi_n\left(Dk_n+\alpha\right)}, \tag{33}$$

while ϕ_n can be rewritten as

$$\phi_n = 2\frac{\left(D^2 k_n^2 + \alpha n_*^2 k_*\right)\sinh(k_n h) + \left(Dk_n n_*^2 k_* + Dk_n \alpha\right)\cosh(k_n h)}{Dk_n+\alpha}.$$

The fraction in (33) is always positive for positive D, k_n, α, h, k_*. This means that signs of L_n^{ch} and L_n^{ph} always coincide.

If a stress-induced phase transition problem is considered, for which the velocity is defined by Eq. (11), similar analysis of a perturbed boundary gives the following kinetics for the amplitude of the perturbations

$$\frac{1}{k_{\text{ph}}}\frac{\mathrm{d}\xi_n}{\mathrm{d}t} = L_n^{\text{ph}}\xi_n. \tag{34}$$

Since ξ_n is the amplitude of the nth harmonic of the front perturbation, multipliers L_n^{ch} and L_n^{ph} are proportional to the exponential growth factor of the harmonic for the chemo-mechanical and the phase transition problems, respectively. For both problems, the sign of these multiplies defines the behavior of the solution — if the sign is negative for each n, the perturbations decay in time. If at least one L_n is positive, then the perturbation with wave number k_n grows exponentially, which leads to the instability of the interface.

Since L_n^{ch} and L_n^{ph} have identical signs, the stability of a phase boundary in the analogous phase transition problem necessarily results in the stability of a chemical reaction front in the chemo-mechanical problem. Therefore, the diffusive reactant does not influence the stability of the planar front — the diffusion process cannot stabilize the unstable front and similarly otherwise. This makes it possible to reduce the analysis of the reaction front stability to the analysis of the stability

of the phase boundaries carried out earlier (e.g., Grinfeld, 1991; Fried, 1992, 1993; Fu and Freidin, 2004). It should also be noted that the necessary criterion of the stability of an arbitrary phase interface is the stability of planar reaction fronts corresponding to various points of the examined interface (Gurtin, 1983).

4.1. Influence of loading and material parameters on stability of the planar front

As outlined in Section 4, functions $A_n^{\pm}$, $B_n^{\pm}$, $C_n^{\pm}$, $D_n^{\pm}$ should be found by solving the system of equations consisting of the boundary and the interface conditions of BVP (15). These functions are needed to obtain L_n^{ph}. The difficulty with solving the aforementioned system is that with growing n, the system becomes ill-conditioned. This means that for higher wave numbers, an accurate numerical solution of this system cannot be guaranteed.

The solution of the equations to obtain L_n^{ph} and L_n^{ch} for given problem parameters has been implemented in a small Matlab code.[1] It should also be mentioned that for all parameter sets, considered by the authors, the absolute values of L_n^{ph} increased with n for both stable and unstable configurations. If such behavior is general, i.e., $\left|L_n^{\text{ph}}\right|$ increases with n for $n > n_0$, then it should be sufficient to calculate first n_0 values of L_n^{ph} to verify this necessary stability criterion.

Using the developed methodology of the linear stability analysis, it is possible to obtain stability regions in the space of material and loading parameters. Since it has been shown that the diffusion parameters of the model do not influence the stability behavior, L_n^{ph} has been calculated. The Poisson's ratios were fixed (the values are given below); the Young's modulus of the untransformed material was taken to be $E_- = 60$; the externally-applied displacement was taken to be $u_0 = 0.02$. With this, the parametric space of the problem is defined by ratio E_+/E_-, chemical transformation θ and chemical energy γ. For simplicity, γ was selected such that the equilibrium position is always exactly at $h = 0.5$. From the physical point of view, the variation of γ may correspond to the variation of the temperature.

By varying E_+/E_- and θ, one can obtain areas, where the values of L_1^{ph} are positive or negative, as illustrated in Fig. 4, left. The ratio of the Young's moduli is varied from 0.5 to 3, which is a reasonable range that covers some cases, e.g., Morozov et al. (2020), and parameter θ is varied from 0 to 0.05 to be consistent with the small-strains approach. The corresponding values of energy parameter γ are shown in Fig. 4, right.

The values of L_n^{ph} also depend on the Poisson's ratio. This is demonstrated in Fig. 5 that presents contour plots showing L_1^{ph} as a function of E_+/E_- and θ, similarly to Fig. 4, left, but for different sets of the Poisson's ratios. The variation of the Poisson's ratios changes quantitatively the stability zones in the parametric space, which can be seen from the positions of the black lines (corresponds to $L_1^{\text{ph}} = 0$), although qualitatively the behavior of L_1^{ph} in the parametric space is similar for all considered sets of the Poisson's ratios.

Since the linear stability analysis criterion is only a necessary criterion, regions where $L_1^{\text{ph}} > 0$ correspond to the system being unstable, while regions where $L_1^{\text{ph}} \leq 0$ require additional verification for $n \geq 2$. Using these results, the provisionally stable and the unstable configurations were selected for the further numerical study, Section 6.

5. Numerical approaches for moving chemical reaction fronts

As outlined in the introduction, the classical remeshing procedure is a successful approach for modeling kinetics of the chemical reaction fronts (Freidin et al., 2016, 2022), including an approach to an equilibrium (Morozov, 2021). The procedure, however, has its own

---

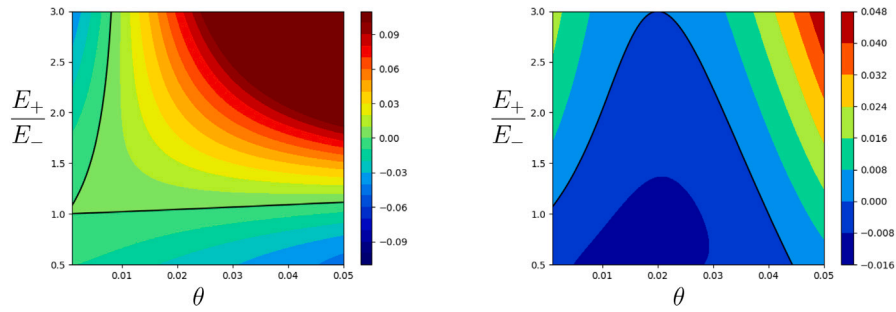[1] The code is available upon request.

Fig. 4. The values of operator L_1^{ph} (left) and the corresponding values of γ (right) in the material parameter space. Solid black lines represent $L_1^{ph} = 0$ level in the left subfigure and $\gamma = 0$ level in the right subfigure. The Poisson's ratios $\nu_+ = \nu_- = 0.25$ are used.
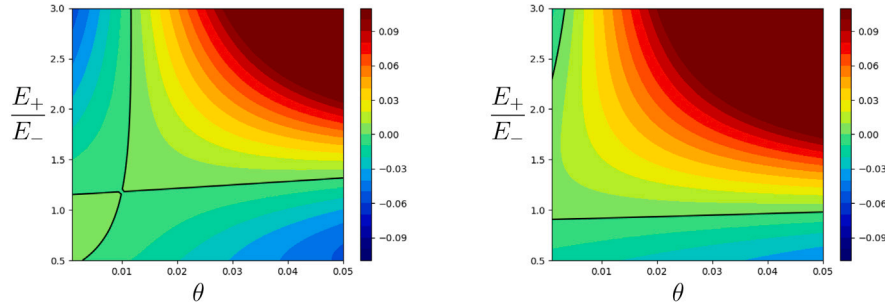

Fig. 5. The values of operator L_1^{ph} in the material parameter space for different values of the Poisson's ratios: left subfigure for $\nu_- = 0.1$ and $\nu_+ = 0.3$; right subfigure for $\nu_- = 0.3$ and $\nu_+ = 0.15$. Solid black lines represent $L_1^{ph} = 0$ level.

disadvantages and one of the aims of the present paper is to compare it with the recently-proposed extension of the CutFEM approach to chemo-mechanics (Poluektov and Figiel, 2019). For the details of the numerical approaches the reader is referred to the corresponding publications. Since the comparison is performed for linear elasticity, the CutFEM-based method has been simplified to a linear elastic setting. Furthermore, the calculation of stresses and strains to model the interface kinetics has been changed from the approach given in Section 4.4.2 of Poluektov and Figiel (2019) to the new method that is given below.

Although the details of the numerical procedures are given in Morozov (2021) and Poluektov and Figiel (2019), it can be useful to outline the general concept of the numerical approach to the chemo-mechanical problem. In both approaches, the chemical reaction front is computationally represented by a set of points in 2D, connected by line segments. An explicit time stepping is used to move the front, which implies that for a given position of the front, velocity V_{Γ_*} at each point must be calculated and then used to move the points of the front by $V_{\Gamma_*}\Delta t$ along the normal to the front, where Δt is the time step. The normal at a point is defined as a weighted average of the normals to the adjacent line segments. To calculate the velocity at each point, the stresses, the strains and the concentration are required. Therefore, at each time step, given the configuration (position) of the front, Eq. (3) with the corresponding boundary and interface conditions is solved first and the stresses and strains are found. Then, Eq. (5) with the corresponding boundary conditions is solved, where the stresses and strains enter boundary condition (6). This gives the concentration at the front and allows calculating the velocity of the front. Using the latter, the new configuration of the front is calculated (i.e., for the next time step). The difference between the considered numerical approaches consists in how the PDEs are solved — either on the cut mesh with weakly-enforced boundary/interface conditions or on the mesh that is newly generated at each time step.

5.1. Calculation of stresses and strains for interface movement

To calculate the interface velocity, given by expression (2), the stresses and strains at the interface points must be evaluated. Previously

(Section 4.4.2 of Poluektov and Figiel, 2019), a simple inter-element averaging procedure to calculate these stresses and strains has been proposed (it will be referred to as the old procedure). Since then, a more accurate procedure has been implemented and is described below.

The old procedure takes directly the finite-element stresses and strains of the elements adjacent to the interface point and averages them. The problem with this is that the directly calculated finite-element stresses and strains are of a "bad quality" — they have worse convergence rate than the displacements. Meanwhile, the simulations discussed in the present paper use one of the major advantages of the CutFEM approach — they are performed on a structured mesh. This can be used to calculate more accurate stresses and strains. It should be emphasized that this is a postprocessing step, not the actual solution of the linear momentum balance equation.

After the nodal solution is obtained (i.e., the displacements are obtained using the CutFEM method), the gradient of the displacements is calculated at each node by finite differences, using the fact that the mesh is structured. In the current implementation of the procedure, the second-order accurate first derivatives of the displacements are calculated. For example, $\partial u_x^i / \partial x$ at node i is approximated by $\left(u_x^{i+1} - u_x^{i-1}\right)/2\Delta x$, where u_x^{i+1} and u_x^{i-1} are the displacements at the nodes to the right and to the left of node i, respectively. If node i is at a boundary, a three-point stencil and forward/backward finite-difference is used. Similarly for other derivatives, which form the gradient of the displacements. Then, the gradients of the displacements at the nodes can be used to calculate the gradients at the intersection points of the interface and the mesh by simple linear interpolation between the nodes along the element edges. Having the gradients of the displacements, the stresses and strains can be calculated. The main advantage of this procedure is that the obtained quantities at the nodes are second-order accurate, if the linear elements are used.

6. Numerical results for the chemical reaction front kinetics

The CutFEM-based and the remeshing methods are compared in three different examples. The first example is the propagation of a flat
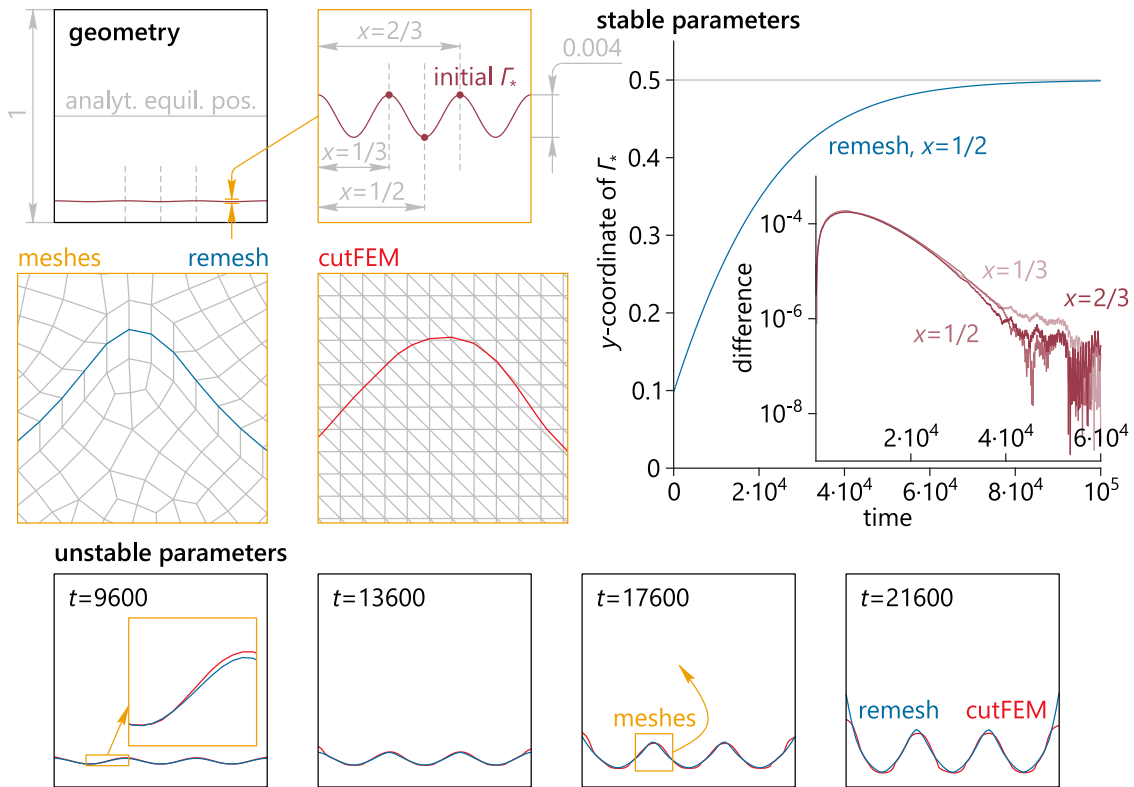
Fig. 6. Propagation of a chemical reaction front in a 2D body for two different cases — the stable and the unstable behavior, which differ by the set of material parameters and the loading. Initial configuration of the chemical reaction front (upper left) is identical for both cases and has a small perturbation. The stable case is illustrated by the evolution of the y-coordinate of the central point of the interface. The CutFEM and the remeshing solutions at three interface points are compared (right, inset). The unstable case is illustrated by four snapshots of the reaction front at different times (bottom). Cropped examples of the finite-element meshes are shown for one of the snapshots (center left).

reaction front, with an initially applied perturbation, in a 2D geometry with plane strain formulation. To investigate the performance of the methods, two different scenarios are considered — stable and unstable behavior (material parameters are given below). The flat reaction front with a perturbation is initiated far from the equilibrium position. In the case of equilibrium being stable, the perturbation diminishes and the front approaches the equilibrium position. When the selected elastic material constants correspond to the equilibrium being unstable, the amplitude of the perturbation grows (exponentially, as shown analytically in Section 4), even before the front approaches the equilibrium position. Both scenarios are illustrated in Fig. 6.

For the stable case, the time-evolution of the reaction front is shown by plotting the y-coordinate of the central point of the interface (only one point is selected because the difference between the y-coordinates of the points of the interface becomes invisible due to the decay of the initial perturbation). To compare the CutFEM and the remeshing solutions, three different points of the interface $x = 1/3, 1/2, 2/3$ are selected. The absolute difference between the positions of the points resulting from two methods is shown in the inset, which is in the range of 10^{-4} to 10^{-6}.

For the unstable case, the time-evolution of the reaction front is shown by snapshots of the front configuration at four different moments of time. It can be seen that the discrepancy between the methods accumulates with time and is mostly revealed at the boundaries of the domain. This is related to the instability of the interface — as any perturbation of the front should grow in time, a numerical perturbation (i.e., a numerical error) also grows in time. The discrepancy at the edges of the domain is related to slightly different ways of calculating stresses and strains at the interface.

For this example, $H = L = 1$ are taken. A plane-strain formulation is considered. The initial position of the front is described by the following equation: $y = 0.1 + 0.002 \cos(6\pi x)$. The transformation strain

is taken to be $\theta = 0.01$. For the stable case, the Lamé parameters of the materials and the applied displacement are taken to be $\mu_+ = 58$, $\mu_- = 26$, $\lambda_+ = 50$, $\lambda_- = 10$, $u_0 = 0.0453$. For the unstable case, the parameters are taken to be $\mu_+ = 50$, $\mu_- = 66$, $\lambda_+ = 66$, $\lambda_- = 34$, $u_0 = -0.0381$. Since the chemical and the diffusion parameters do not affect the stability of the interface at the equilibrium position, only one set of the following chemical and diffusion parameters is used: $\alpha/D = 2$, $k_*/D = 0.1$, $\gamma = 0.05$, $n_- M_-/(\rho_- RT) = 0.0177$, $k_* c_* n_- M_-/\rho_- = 0.0432$, $n_* = 1$. For the CutFEM, the mesh consisting of linear elements in the form of isosceles right triangle with the side of Δx is used. In the remeshing procedure, linear quads with full integration are used, while the size of an element is approximately equal to Δx. Parameter $\Delta x = 1/64$ is taken. Time steps of $\Delta t = 80$ and $\Delta t = 160$ are taken for the stable and unstable cases, respectively. For the CutFEM, numerical parameters, which were denoted as λ and κ in Poluektov and Figiel (2019), are taken to be 10^4 and 10^{-2}, respectively. The boundary conditions given by Eqs. (19)–(23) are used.

The second considered case is similar to the first example. However, additional shear displacements are applied at the top boundary. This creates a shear stress state; therefore, if the initial position of the interface is horizontal, in the case of stable parameters, the interface should rotate as it approaches the equilibrium position. Exactly this is observed in the results of numerical simulations shown in Fig. 7. The time-evolution of the reaction front is shown by plotting the y-coordinate of three different points of the interface, which have $x = 1/5, 1/2, 4/5$, for both approaches. Furthermore, the snapshots of the front configuration at four different moments of time are plotted. As in the previous example, both approaches give close results; small discrepancies can be attributed to a different way of calculating stresses and strains at the interface within the approaches.

For this example, the initial position is taken to be line $y = 0.1$. All other parameters are taken to be the same as in the stable case of
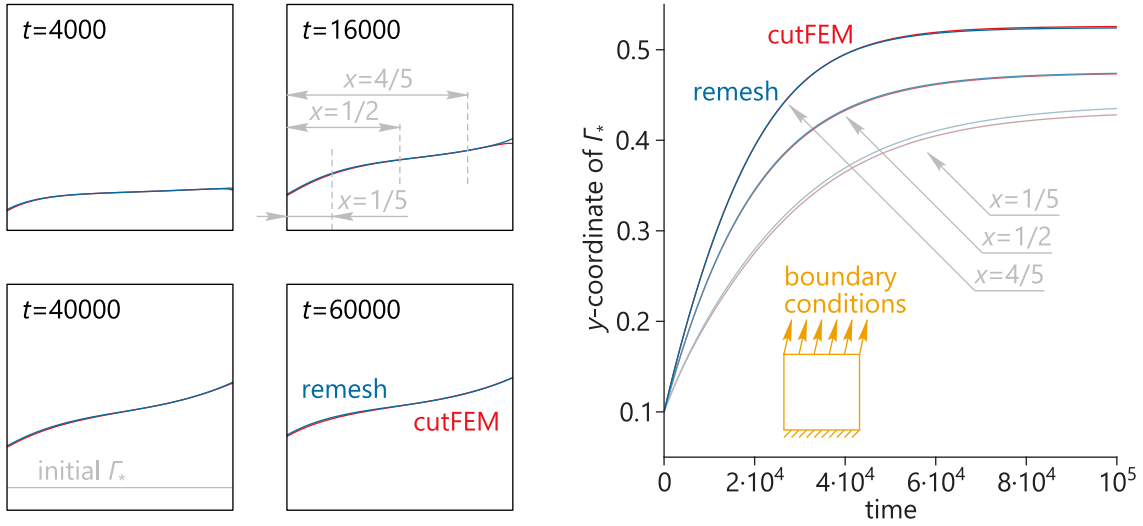
Fig. 7. Propagation of a chemical reaction front in a 2D body with applied shear loading. The kinetics is illustrated by the evolution of the *y*-coordinate of three points of the front (right), as well as by four snapshots of the reaction front at different times (left). The initial configuration of the chemical reaction front is shown in the lower-left snapshot. The loading case is schematically illustrated in the inset (right).

the first example. For the mechanical problem, the following boundary conditions are used: the clamped bottom boundary, the stress-free left and right boundaries, the prescribed displacements at the top boundary, $\vec{u}_- = u_0 \vec{e}_y + 0.01 \vec{e}_x$. For the diffusion problem, the same boundary conditions as in the previous example are used.

The third example focuses on a different topology of the reaction front — a closed curve. The outer material is the chemically transformed phase, the inner — the untransformed phase. In the previous study of chemical reaction front stability (Morozov, 2021), cylindrical geometries have been considered and a set of parameters leading to a stable configuration of the circular reaction front have been established. In the present paper, the geometry is changed to a square, which creates inhomogeneous stress distributions (with respect to the polar angle in the polar coordinate system), and, therefore, leads to a more complex equilibrium configuration. To highlight the effect of stresses on the equilibrium configuration of the front, two different loading cases are considered — biaxial stretching and piecewise-linear prescribed displacements. Thus, for the mechanical part of the problem, for the first loading case, the following boundary conditions are prescribed:

$$\vec{u}_+ \cdot \vec{e}_y = 0 \quad \text{at } y = 0, \qquad \vec{u}_+ \cdot \vec{e}_y = u_0 \quad \text{at } y = H,$$

$$\vec{u}_+ \cdot \vec{e}_x = 0 \quad \text{at } x = 0, \qquad \vec{u}_+ \cdot \vec{e}_x = u_0 \quad \text{at } x = L, \qquad u_0 = 0.076,$$

and $\boldsymbol{\sigma}_+ : \vec{e}_x \vec{e}_y = 0$ on all boundaries. For the second loading case, the following displacements are prescribed on the boundaries:

$$\vec{u}_+ = 0.025\,(x-1)\,\vec{e}_x + 0.025\left(\vec{N}\cdot\vec{e}_y\right)(|x-1|+1)\,\vec{e}_y \text{ at } y = 0 \text{ and } y = H,$$

$$\vec{u}_+ = -0.025\left(\vec{N}\cdot\vec{e}_x\right)(|y-1|+2)\,\vec{e}_x + 0.05\,(y-1)\,\vec{e}_y \text{ at } x = 0 \text{ and } x = L.$$

For the diffusion problem, the mixed boundary condition, Eq. (7), is prescribed on all boundaries.

The initially circular configuration of the front evolves into two different shapes for these two loading scenarios, which are illustrated in Fig. 8. As in the previous examples, during the initial stage (fast kinetics), both methods produce indistinguishable results.

At the final stage, i.e., close to the equilibrium configuration (when the velocity of the front becomes relatively small), the CutFEM-based approach produces an artefact — some parts of the front tend to align with the nearest element edges. There might be several reasons for this. The first reason may come from the numerical error in the stresses and strains (i.e., from the numerical error in the derivative of the solution of the finite-element problem), which enters the expression for the velocity. When the stress and strain dependency has been excluded from the kinetics (results are not shown), this artefact disappeared.
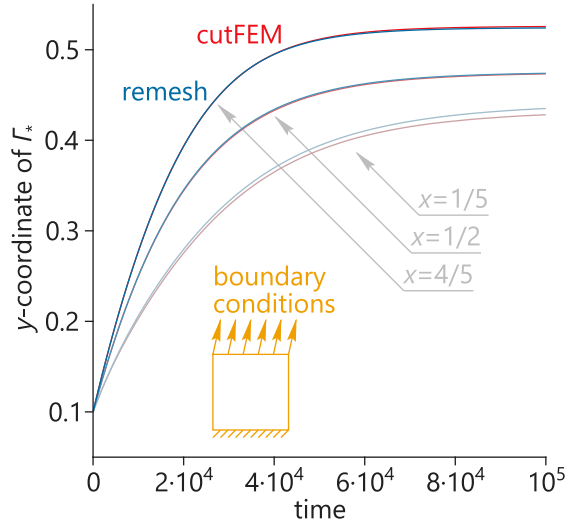
It should be emphasized that the new procedure of extracting the stresses and strains (outlined in Section 5.1) results in the second-order accurate quantities relying on the structured mesh, and due to this procedure, only small sections of the front are subjected to this artefact, as seen in Fig. 8 at $t = 15000$. If the new procedure is not used and simple inter-element stress and strain averaging is utilized (as described in Section 4.4.2 of Poluektov and Figiel, 2019), the artefact is much more severe (results are not shown) — the entire reaction front aligns with the nearest element edges at the equilibrium position. It can be concluded that the order of elements, hence the accuracy of the stresses and strains, is related to the emergence of this artefact, and higher-order elements may lead to a more smooth numerically-obtained reaction front at the equilibrium. It should also be noted that there are other post-processing methods, e.g., Payen and Bathe (2011, 2012), not relying on the structured mesh and that can extract the stresses and strains of a higher quality than ones given by a direct finite-element solution.

The second reason for the emergence of the artefact may be the numerical error in the normal to the front. In the current implementation, the front is a piecewise-linear curve; it is linear within each element and changes slope at the intersection points with the mesh. The normal at an intersection point is defined as a weighted average of the normals to the adjacent line segments. More elaborate ways of representing the front, such as by using the level-set method, as was done in Burman et al. (2018), may also lead to a more smooth reaction front at the equilibrium.

For this example, $H = L = 2$ are taken. The initial position is taken to be a circle with radius 0.73 in the middle of the square domain. The transformation strain is taken to be $\theta = 0.1$. The Lamé parameters of the materials are taken to be $\mu_+ = 10.0$, $\mu_- = 24.4$, $\lambda_+ = 24.9$, $\lambda_- = 58.6$. The same chemical and diffusion parameters are used as in the first example, apart from $\gamma = -0.15$. The time step of $\Delta t = 50$ is taken. For the CutFEM-based approach, spatial step of $\Delta x = 1/32$ is taken, for the remeshing approach, $\Delta x \approx 0.0116$ is taken for the first loading case and $\Delta x \approx 0.0077$ is taken for the second loading case.

7. Conclusions and outlook

The stability problem of the planar chemical reaction front was studied using analytical and numerical approaches. In the analytical approach, the linearized perturbed boundary value problem was solved. The kinetics of the stress-dependent localized chemical reaction
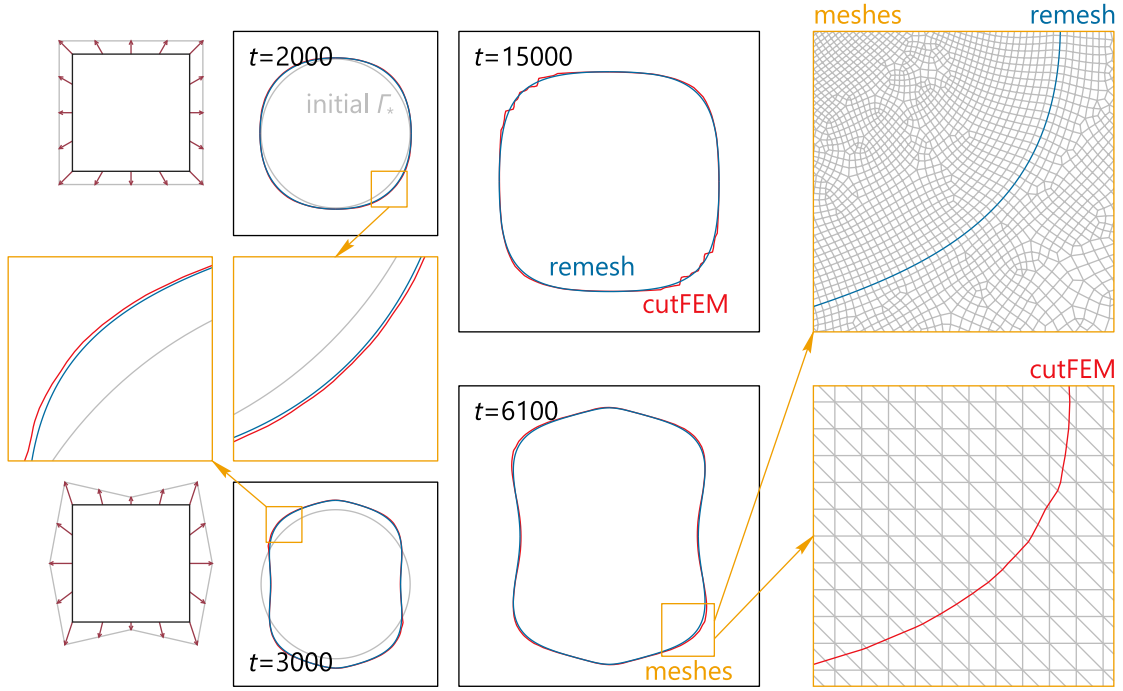
Fig. 8. The intermediate and the final configurations of a closed-curve reaction front in a 2D body (center) under two different loading conditions. The loading conditions as well as the initial configurations of the front are illustrated schematically (left). Cropped examples of the finite-element meshes are shown for the second loading scenario (right).

was modeled using the chemical affinity tensor approach. For mathematically similar models of phase transitions and localized chemical reactions, it was shown that in the case of a planar interface and the chosen constitutive law for the reaction rate, the diffusion parameters do not affect the stability of the equilibrium configuration, i.e., the stability of the interface is defined entirely by the mechanical properties of the materials in both phase and chemical transformation problems. Based on this, the stability regions in the space of the material and the loading parameters were obtained. The "stable" and "unstable" parameters were used to validate the developed numerical procedures.

In the numerical treatment of the problem, two approaches for modelling of the chemical reaction front propagation were considered. Both the CutFEM-based and the remeshing methods show the same kinetics of the sharp reaction front and are able to capture its stability behavior. However, when the interface approaches the reaction blocking state, the CutFEM-based approach can produce minor artefacts, when some parts of the interface tend to align with the nearest element boundary. The inaccuracy in the interface position is order of the element size. As for the remeshing procedure, it requires more implementational effort for tracking the position of the interface, e.g., writing scripts to handle the intersections of the front with the geometry and with itself. In addition, for all studied cases, regeneration of the mesh at each iteration took more computational time than the actual solution of the finite-element problem. Nevertheless, both studied methods can be used to model the chemical reaction front kinetics and to analyze the stability of the interface propagation. The developed numerical tools can now be used to investigate the stability of phase boundaries and chemical reaction fronts in materials with more complex constitutive behavior and undergoing large deformations.

Declaration of competing interest

The authors declare that they have no known competing financial interests or personal relationships that could have appeared to influence the work reported in this paper.

Data availability

Data will be made available on request.

Acknowledgments

Appendix. Derivation of the perturbation of the mechanical energy

Using the perturbation of the interface, Eq. (12), it can be written that for any field a defined in volume Ω_+ or Ω_-, its value at the position of the perturbed interface can be expressed via its value at the position of the unperturbed interface as

$$a|_{\vec{R}_*} = a|_{\vec{R}_*^0} + \eta \vec{N}_*^0 \cdot \nabla a|_{\vec{R}_*^0} + O\left(\eta^2\right). \tag{35}$$

When the stresses and strains are considered, for the perturbed problem, the entire fields are affected by the perturbation of the displacements, Eq. (13), resulting in

$$\boldsymbol{\sigma}_\pm = \boldsymbol{\sigma}_\pm\left(\vec{u}_\pm\right) = \boldsymbol{\sigma}_\pm\left(\vec{u}_\pm^0 + \vec{w}_\pm\right) = \boldsymbol{\sigma}_\pm^0 + \boldsymbol{\sigma}_\pm\left(\vec{w}_\pm\right), \tag{36}$$

$$\boldsymbol{\varepsilon}_\pm = \boldsymbol{\varepsilon}_\pm^0 + \boldsymbol{\varepsilon}_\pm\left(\vec{w}_\pm\right). \tag{37}$$

The values of these fields at the position of the perturbed interface are substituted into mechanical energy χ, Eq. (9). These values can be expressed via the values of these fields at the position of the unperturbed interface as

$$\boldsymbol{\sigma}_\pm|_{\vec{R}_*} = \left(\boldsymbol{\sigma}_\pm^0 + \boldsymbol{\sigma}_\pm\left(\vec{w}_\pm\right) + \eta\vec{N}_*^0 \cdot \nabla\boldsymbol{\sigma}_\pm^0\right)\Big|_{\vec{R}_*^0} + O\left(\eta^2\right) =$$
$$= \left(\boldsymbol{\sigma}_\pm^0 + \boldsymbol{\sigma}_\pm^\delta\right)\Big|_{\vec{R}_*^0} + O\left(\eta^2\right), \tag{38}$$

$$\boldsymbol{\varepsilon}_\pm|_{\vec{R}_*} = \left(\boldsymbol{\varepsilon}_\pm^0 + \boldsymbol{\varepsilon}_\pm\left(\vec{w}_\pm\right) + \eta\vec{N}_*^0 \cdot \nabla\boldsymbol{\varepsilon}_\pm^0\right)\Big|_{\vec{R}_*^0} + O\left(\eta^2\right) =$$
$$= \left(\boldsymbol{\varepsilon}_\pm^0 + \boldsymbol{\varepsilon}_\pm^\delta\right)\Big|_{\vec{R}_*^0} + O\left(\eta^2\right), \tag{39}$$

where $\boldsymbol{\sigma}_\pm^\delta$ and $\boldsymbol{\varepsilon}_\pm^\delta$ are introduced to shorten the notation. Now, these values can be substituted into χ. In the following derivation, $\vec{R}_*^0$ is omitted starting from the second line. The value of χ can be transformed as

follows:

$$\chi = \gamma + \left(\frac{1}{2}\boldsymbol{\sigma}_- : \boldsymbol{\varepsilon}_- - \frac{1}{2}\boldsymbol{\sigma}_+ : (\boldsymbol{\varepsilon}_+ - \boldsymbol{\varepsilon}^{\mathrm{ch}}) + \boldsymbol{\sigma}_+ : (\boldsymbol{\varepsilon}_+ - \boldsymbol{\varepsilon}_-) \right)\Big|_{\vec{R}_*} =$$

$$= \gamma + \frac{1}{2}\boldsymbol{\sigma}_-^0 : \boldsymbol{\varepsilon}_-^0 + \frac{1}{2}\boldsymbol{\sigma}_-^0 : \boldsymbol{\varepsilon}_-^\delta + \frac{1}{2}\boldsymbol{\sigma}_-^\delta : \boldsymbol{\varepsilon}_-^0 + \frac{1}{2}\boldsymbol{\sigma}_+^0 : (\boldsymbol{\varepsilon}_+^0 + \boldsymbol{\varepsilon}^{\mathrm{ch}}) +$$

$$+ \frac{1}{2}\boldsymbol{\sigma}_+^0 : \boldsymbol{\varepsilon}_+^\delta + \frac{1}{2}\boldsymbol{\sigma}_+^\delta : (\boldsymbol{\varepsilon}_+^0 + \boldsymbol{\varepsilon}^{\mathrm{ch}}) - \boldsymbol{\sigma}_+^0 : \boldsymbol{\varepsilon}_-^0 - \boldsymbol{\sigma}_+^0 : \boldsymbol{\varepsilon}_-^\delta - \boldsymbol{\sigma}_+^\delta : \boldsymbol{\varepsilon}_-^0 +$$

$$+ O\left(\eta^2\right) = \chi^0 - [\![\boldsymbol{\sigma}^0]\!] : \boldsymbol{\varepsilon}_-^\delta + [\![\boldsymbol{\varepsilon}^0]\!] : \boldsymbol{\sigma}_+^\delta + O\left(\eta^2\right) = \chi^0 -$$

$$- [\![\boldsymbol{\sigma}^0]\!] : \left(\boldsymbol{\varepsilon}_- (\vec{w}_-) + \eta \vec{N}_*^0 \cdot \nabla \boldsymbol{\varepsilon}_-^0 \right) + [\![\boldsymbol{\varepsilon}^0]\!] : \left(\boldsymbol{\sigma}_+ (\vec{w}_+) + \eta \vec{N}_*^0 \cdot \nabla \boldsymbol{\sigma}_+^0 \right) +$$

$$+ O\left(\eta^2\right),$$

where χ^0 is the value of χ at the unperturbed state.

References

Abali, B.E., 2020. Modeling mechanochemistry in Li-ion batteries. In: Nicosia, G., Romano, V. (Eds.), Scientific Computing in Electrical Engineering. Springer Nature Switzerland AG, pp. 79–91.

Abeyaratne, R., Knowles, J.K., 1991. Kinetic relations and the propagation of phase boundaries in solids. Arch. Ration. Mech. Anal. 114, 119–154.

Abeyaratne, R., Knowles, J.K., 2006. Evolution of Phase Transitions: A Continuum Theory. Cambridge University Press.

Ahmad, Z., Viswanathan, V., 2017. Stability of electrodeposition at solid-solid interfaces and implications for metal anodes. Phys. Rev. Lett. 119, 056003.

Anders, D., Hesch, C., Weinberg, K., 2012. Computational modeling of phase separation and coarsening in solder alloys. Int. J. Solids Struct. 49 (13), 1557–1572.

Arafat, Y., Yang, H., Dutta, I., Kumar, P.A., Datta, B., 2020. A model for intermetallic growth in thin Sn joints between Cu substrates: Application to solder microjoints. J. Electron. Mater. 49, 3367–3382.

Barvosa-Carter, W., Aziz, M.J., Gray, L.J., Kaplan, T., 1998. Kinetically driven growth instability in stressed solids. Phys. Rev. Lett. 81 (7), 1445–1448.

Barvosa-Carter, W., Aziz, M.J., Phan, A.V., Kaplan, T., Gray, L.J., 2004. Interfacial roughening during solid phase epitaxy: Interaction of dopant, stress, and anisotropy effects. J. Appl. Phys. 96 (10), 5462–5468.

Berezovski, A., Engelbrecht, J., Maugin, G.A., 2008. Numerical Simulation of Waves and Fronts in Inhomogeneous Solids. World Scientific.

Berezovski, A., Maugin, G.A., 2005. Stress-induced phase-transition front propagation in thermoelastic solids. Eur. J. Mech. — A/Solids 24, 1–21.

Böhme, T., Müller, W.H., Weinberg, K., 2009. Numerical modeling of diffusion induced phase transformations in mechanically stressed lead-free alloys. Comput. Mater. Sci. 45 (3), 837–844.

Brassart, L., Suo, Z., 2012. Reactive flow in large-deformation electrodes of lithium-ion batteries. Int. J. Appl. Mech. 4 (3), 1250023.

Brassart, L., Suo, Z., 2013. Reactive flow in solids. J. Mech. Phys. Solids 61 (1), 61–77.

Burman, E., Elfverson, D., Hansbo, P., Larson, M.G., Larsson, K., 2018. Shape optimization using the cut finite element method. Comput. Methods Appl. Mech. Engrg. 328, 242–261.

Burman, E., Elfverson, D., Hansbo, P., Larson, M.G., Larsson, K., 2019a. Cut topology optimization for linear elasticity with coupling to parametric nondesign domain regions. Comput. Methods Appl. Mech. Engrg. 350, 462–479.

Burman, E., Elfverson, D., Hansbo, P., Larson, M.G., Larsson, K., 2019b. Hybridized CutFEM for elliptic interface problems. SIAM J. Sci. Comput. 41 (5), A3354–A3380.

Burman, E., Hansbo, P., 2012. Fictitious domain finite element methods using cut elements: II. A stabilized Nitsche method. Appl. Numer. Math. 62 (4), 328–341.

Büttner, C.C., Zacharias, M., 2006. Retarded oxidation of Si nanowires. Appl. Phys. Lett. 89 (26), 263106.

Cui, Z.W., Gao, F., Qu, J.M., 2012. A finite deformation stress-dependent chemical potential and its applications to lithium ion batteries. J. Mech. Phys. Solids 60 (7), 1280–1295.

Cui, Z.W., Gao, F., Qu, J.M., 2013. Interface-reaction controlled diffusion in binary solids with applications to lithiation of silicon in lithium-ion batteries. J. Mech. Phys. Solids 61 (2), 293–310.

Doux, J.-M., Nguyen, H., Tan, D.H.S., Banerjee, A., Wang, X., Wu, E.A., Jo, C., Yang, H., Meng, Y.S., 2020. Stack pressure considerations for room-temperature all-solid-state lithium metal batteries. Adv. Energy Mater. 10 (1), 1903253.

Duddu, R., Chopp, D.L., Voorhees, P., Moran, B., 2011. Diffusional evolution of precipitates in elastic media using the extended finite element and the level set methods. J. Comput. Phys. 230 (4), 1249–1264.

Eremeev, V.A., Freidin, A.B., Sharipova, L.L., 2003. Nonuniqueness and stability in problems of equilibrium of elastic two-phase bodies. Doklady Phys. 48 (7), 359–363.

Eumelen, G.J.A.M., Bosco, E., Suiker, A.S.J., Hermans, J.J., 2023. Chemo-mechanical model for degradation of oil paintings by amorphous and crystalline metal soaps. Eur. J. Mech. — A/Solids 97, 104827.

Eumelen, G.J.A.M., Bosco, E., Suiker, A.S.J., van Loon, A., Iedema, P.D., 2019. A computational model for chemo-mechanical degradation of historical oil paintings due to metal soap formation. J. Mech. Phys. Solids 132, 103683.

Freidin, A.B., 2013. Chemical affinity tensor and stress-assist chemical reactions front propagation in solids. In: Proceedings of the ASME 2013 International Mechanical Engineering Congress and Exposition. Volume 9: Mechanics of Solids, Structures and Fluids. V009T10A102.

Freidin, A.B., Korolev, I.K., Aleshchenko, S.P., 2022. FEM-simulations of a chemical reaction front propagation in an elastic solid with a cylindrical hole. In: Polyanskiy, V.A., Belyaev, A.K. (Eds.), Mechanics and Control of Solids and Structures. Springer International Publishing, pp. 195–208.

Freidin, A.B., Korolev, I.K., Aleshchenko, S.P., Vilchevskaya, E.N., 2016. Chemical affinity tensor and chemical reaction front propagation: Theory and FE-simulations. Int. J. Fract. 202 (2), 245–259.

Freidin, A.B., Sharipova, L.L., Cherkaev, A.V., 2021. On equilibrium two-phase microstructures at plane strain. Acta Mech. 232 (5), 2005–2021.

Freidin, A.B., Vilchevskaya, E.N., 2020. Chemical affinity tensor in coupled problems of mechanochemistry. In: Altenbach, H., Öchsner, A. (Eds.), Encyclopedia of Continuum Mechanics. Springer, Berlin, Heidelberg.

Freidin, A.B., Vilchevskaya, E.N., Korolev, I.K., 2014. Stress-assist chemical reactions front propagation in deformable solids. Internat. J. Engrg. Sci. 83, 57–75.

Fried, E., 1992. Stability of a two-phase process involving a planar phase boundary in a thermoelastic solid. Contin. Mech. Thermodyn. 4 (1), 59–79.

Fried, E., 1993. Stability of a two-phase process in an elastic solid. J. Elasticity 31 (3), 163–187.

Fu, Y.B., Freidin, A.B., 2004. Characterization and stability of two-phase piecewise-homogeneous deformations. Proc. R. Soc. A: Math. Phys. Eng. Sci. 460, 3065–3094.

Gao, T., Lu, W., 2022. Surface instability of metal anode in all-solid-state batteries. Int. J. Solids Struct. 253, 111790.

Glansdorff, P., Prigogine, I., 1971. Thermodynamic Theory of Structure, Stability and Fluctuations. John Wiley & Sons Ltd.

Grinfeld, M., 1991. Thermodynamic Methods in the Theory of Heterogeneous Systems. Longman Sc & Tech.

Gross, D., Müller, R., Kolling, S., 2002. Configurational forces — morphology evolution and finite elements. Mech. Res. Commun. 29 (6), 529–536.

Gurtin, M.E., 1983. Two-phase deformations of elastic solids. Arch. Ration. Mech. Anal. 84 (1), 1–29.

Gurtin, M.E., 2000. Configurational Forces as Basic Concepts of Continuum Physics. Springer-Verlag New York.

Hansbo, A., Hansbo, P., 2002. An unfitted finite element method, based on Nitsche's method, for elliptic interface problems. Comput. Methods Appl. Mech. Engrg. 191, 5537–5552.

Hansbo, P., Larson, M.G., Larsson, K., 2017. Cut finite element methods for linear elasticity problems. In: Bordas, S.P.A., Burman, E., Larson, M.G., Olshanskii, M.A. (Eds.), Geometrically Unfitted Finite Element Methods and Applications. Springer International Publishing, pp. 25–63.

Heidemeyer, H., Single, C., Zhou, F., Prins, F.E., Kern, D.P., Plies, E., 2000. Self-limiting and pattern dependent oxidation of silicon dots fabricated on silicon-on-insulator material. J. Appl. Phys. 87 (9), 4580–4585.

Hüter, C., Fu, S., Finsterbusch, M., Figgemeier, E., Wells, L., Spatschek, R., 2017. Electrode-electrolyte interface stability in solid state electrolyte systems: Influence of coating thickness under varying residual stresses. AIMS Mater. Sci. 4 (4), 867–877.

Jia, Z., Li, T., 2015. Stress-modulated driving force for lithiation reaction in hollow nano-anodes. J. Power Sources 275, 866–876.

Jou, H.J., Leo, P.H., Lowengrub, J.S., 1997. Microstructural evolution in inhomogeneous elastic media. J. Comput. Phys. 131 (1), 109–148.

Kao, D.B., McVittie, J.P., Nix, W.D., Saraswat, K.C., 1988. Two-dimensional thermal-oxidation of silicon — II. Modeling stress effects in wet oxides. IEEE Trans. Electron Devices 35 (1), 25–37.

Kim, H.K., Tu, K.N., 1996. Kinetic analysis of the soldering reaction between eutectic SnPb alloy and Cu accompanied by ripening. Phys. Rev. B 53 (23), 16027–16034.

Levitas, V.I., Attariani, H., 2014. Anisotropic compositional expansion in elastoplastic materials and corresponding chemical potential: Large-strain formulation and application to amorphous lithiated silicon. J. Mech. Phys. Solids 69, 84–111.

Liu, I.S., 1992. On interface equilibrium and inclusion problems. Contin. Mech. Thermodyn. 4, 177–186.

Liu, X.H., Fan, F., Yang, H., Zhang, S., Huang, J.Y., Zhu, T., 2013. Self-limiting lithiation in silicon nanowires. ACS Nano 7 (2), 1495–1503.

Liu, X.H., Wang, J.W., Huang, S., Fan, F., Huang, X., Liu, Y., Krylyuk, S., Yoo, J., Dayeh, S.A., Davydov, A.V., Mao, S.X., Picraux, S.T., Zhang, S., Li, J., Zhu, T., Huang, J.Y., 2012. In situ atomic-scale imaging of electrochemical lithiation in silicon. Nature Nanotechnol. 7 (11), 749–756.

Liu, X.H., Zheng, H., Zhong, L., Huan, S., Karki, K., Zhang, L.Q., Liu, Y., Kushima, A., Liang, W.T., Wang, J.W., Cho, J.H., Epstein, E., Dayeh, S.A., Picraux, S.T., Zhu, T., Li, J., Sullivan, J.P., Cumings, J., Wang, C.S., Mao, S.X., Ye, Z.Z., Zhang, S.L., Huang, J.Y., 2011. Anisotropic swelling and fracture of silicon nanowires during lithiation. Nano Lett. 11 (8), 3312–3318.

Marcus, R.B., Sheng, T.T., 1982. The oxidation of shaped silicon surfaces. J. Electrochem. Soc. 129 (6), 1278–1282.

Maugin, G.A., 2010. Configurational Forces: Thermomechanics, Physics, Mathematics, and Numerics. Chapman and Hall/CRC.

McDowell, M.T., Lee, S.W., Nix, W.D., Cui, Y., 2013. 25th anniversary article: Understanding the lithiation of silicon and other alloying anodes for lithium-ion batteries. Adv. Mater. 25 (36), 4966–4984.

Mihalyi, A., Jaccodine, R.J., Delph, T.J., 1999. Stress effects in the oxidation of planar silicon substrates. Appl. Phys. Lett. 74 (14), 1981–1983.

Monroe, C., Newman, J., 2005. The impact of elastic deformation on deposition kinetics at lithium/polymer interfaces. J. Electrochem. Soc. 152 (2), A396.

Morozov, A., 2021. Numerical and analytical studies of kinetics, equilibrium, and stability of the chemical reaction fronts in deformable solids (Ph.D. thesis). Technische Universität Berlin.

Morozov, A., Freidin, A.B., Klinkov, V.A., Semencha, A.V., Müller, W.H., Hauck, T., 2020. Experimental and theoretical studies of Cu-Sn intermetallic phase growth during high-temperature storage of eutectic SnAg interconnects. J. Electron. Mater. 49, 7194–7210.

Morozov, A., Freidin, A.B., Müller, W.H., 2019a. Stability of chemical reaction fronts in the vicinity of a blocking state. PNRPU Mech. Bull. 3, 58–64.

Morozov, A., Freidin, A.B., Müller, W.H., 2023. On stress-affected propagation and stability of chemical reaction fronts in solids. Internat. J. Engrg. Sci. 189, 103876.

Morozov, A., Freidin, A., Müller, W.H., Semencha, A., Tribunskiy, M., 2019b. Modeling temperature dependent chemical reaction of intermetallic compound growth. In: 20th International Conference on Thermal, Mechanical and Multi-Physics Simulation and Experiments in Microelectronics and Microsystems. EuroSimE, Hannover, Germany, pp. 1–8.

Morozov, A., Khakalo, S., Balobanov, V., Freidin, A.B., Müller, W.H., Niiranen, J., 2018. Modeling chemical reaction front propagation by using an isogeometric analysis. Tech. Mech. 38 (1), 73–90.

Muhlstein, C.L., Ritchie, R.O., 2003. High-cycle fatigue of micron-scale polycrystalline silicon films: Fracture mechanics analyses of the role of the silica/silicon interface. Int. J. Fract. 119 (4–2), 449–474.

Muhlstein, C.L., Stach, E.A., Ritchie, R.O., 2002a. Mechanism of fatigue in micron-scale films of polycrystalline silicon for microelectromechanical systems. Appl. Phys. Lett. 80 (9), 1532–1534.

Muhlstein, C.L., Stach, E.A., Ritchie, R.O., 2002b. A reaction-layer mechanism for the delayed failure of micron-scale polycrystalline silicon structural films subjected to high-cycle fatigue loading. Acta Mater. 50 (14), 3579–3595.

Müller, R., Gross, D., 1999. 3D inhomogeneous, misfitting second phase particles-equilibrium shapes and morphological development. Comput. Mater. Sci. 16 (1–4), 53–60.

Natsiavas, P.P., Weinberg, K., Rosato, D., Ortiz, M., 2016. Effect of prestress on the stability of electrode-electrolyte interfaces during charging in lithium batteries. J. Mech. Phys. Solids 95, 92–111.

Nitsche, J., 1971. Über ein Variationsprinzip zur Lösung von Dirichlet-problemen bei Verwendung von Teilräumen, die keinen Randbedingungen unterworfen sind. Abhandlungen aus dem Mathematischen Seminar der Universität Hamburg 36 (1), 9–15.

Ortiz, M., Repetto, E.A., Si, H., 1999. A continuum model of kinetic roughening and coarsening in thin films. J. Mech. Phys. Solids 47 (4), 697–730.

Payen, D.J., Bathe, K.J., 2011. The use of nodal point forces to improve element stresses. Comput. Struct. 89 (5–6), 485–495.

Payen, D.J., Bathe, K.J., 2012. A stress improvement procedure. Comput. Struct. 112, 311–326.

Phan, A.V., Kaplan, T., Gray, L.J., Adalsteinsson, D., Sethian, J.A., Barvosa-Carter, W., Aziz, M.J., 2001. Modelling a growth instability in a stressed solid. Modelling Simul. Mater. Sci. Eng. 9 (4), 309–325.

Poluektov, M., Figiel, L., 2019. A numerical method for finite-strain mechanochemistry with localised chemical reactions treated using a Nitsche approach. Comput. Mech. 63 (5), 885–911.

Poluektov, M., Freidin, A.B., Figiel, L., 2018. Modelling stress-affected chemical reactions in non-linear viscoelastic solids with application to lithiation reaction in spherical Si particles. Internat. J. Engrg. Sci. 128, 44–62.

Prigogine, I., Defay, R., 1954. Chemical Thermodynamics. Longmans, Green.

Qin, L., Wang, K., Xu, H., Zhou, M., Yu, G., Liu, C., Sun, Z., Chen, J., 2020. The role of mechanical pressure on dendritic surface toward stable lithium metal anode. Nano Energy 77, 105098.

Schaefer, M., Fournelle, R.A., Liang, J., 1998. Theory for intermetallic phase growth between Cu and liquid Sn-Pb solder based on grain boundary diffusion control. J. Electron. Mater. 27 (11), 1167–1176.

Schneider, D., Schoof, E., Tschukin, O., Reiter, A., Herrmann, C., Schwab, F., Selzer, M., Nestler, B., 2018. Small strain multiphase-field model accounting for configurational forces and mechanical jump conditions. Comput. Mech. 61 (3), 277–295.

Schneider, D., Schwab, F., Schoof, E., Reiter, A., Herrmann, C., Selzer, M., Böhlke, T., Nestler, B., 2017. On the stress calculation within phase-field approaches: A model for finite deformations. Comput. Mech. 60 (2), 203–217.

Schuß, S., Weinberg, K., Hesch, C., 2018. Thermomigration in SnPb solders: Material model. Mech. Mater. 121, 31–49.

Šilhavý, M., 1997. The Mechanics and Thermodynamics of Continuous Media. Springer-Verlag Berlin Heidelberg.

Socrate, S., Parks, D.M., 1993. Numerical determination of the elastic driving force for directional coarsening in Ni-superalloys. Acta Metall. Mater. 47 (7), 2185–2209.

Su, C.H., Voorhees, P.W., 1996a. The dynamics of precipitate evolution in elastically stressed solids. 1. Inverse coarsening. Acta Mater. 44 (5), 1987–1999.

Su, C.H., Voorhees, P.W., 1996b. The dynamics of precipitate evolution in elastically stressed solids. 2. Particle alignment. Acta Mater. 44 (5), 2001–2016.

Suo, Z., Ortiz, M., Needleman, A., 1992. Stability of solids with interfaces. J. Mech. Phys. Solids 40 (3), 613–640.

Svendsen, B., Shanthraj, P., Raabe, D., 2018. Finite-deformation phase-field chemo-mechanics for multiphase, multicomponent solids. J. Mech. Phys. Solids 112, 619–636.

van Havenbergh, K., Turner, S., Marx, N., van Tendeloo, G., 2016. The mechanical behavior during (de)lithiation of coated silicon nanoparticles as anode material for lithium-ion batteries studied by insitu transmission electron microscopy. Energy Technol. 4 (8), 1005–1012.

Viana, G., Masson, R., Michel, B., Mathieu, B., Gărăjeu, B., 2023. Stress level estimates in coated or uncoated silicon nanoparticles during lithiation. Eur. J. Mech. — A/Solids 100, 105001.

Wang, Y., Wang, Y., Ma, L., Han, J., Guo, F., 2020. Effect of sn grain c-axis on Cu atomic motion in Cu reinforced composite solder joints under electromigration. J. Electron. Mater. 49 (3), 2159–2163.

Wang, Y., Wu, H., Sun, L., Jiang, W., Lu, C., Ma, Z., 2021. Coupled electrochemical-mechanical modeling with strain gradient plasticity for lithium-ion battery electrodes. Eur. J. Mech. — A/Solids 87, 104230.

Weinberg, K., Werner, M., Anders, D., 2018. A chemo-mechanical model of diffusion in reactive systems. Entropy 20 (2), 140.

Wu, H., Xie, Z., Wang, Y., Lu, C., Ma, Z., 2018. Modeling diffusion–induced stress on two-phase lithiation in lithium-ion batteries. Eur. J. Mech. — A/Solids 71, 320–325.

Yeremeyev, V.A., Freidin, A.B., Sharipova, L.L., 2007. The stability of the equilibrium of two-phase elastic solids. J. Appl. Math. Mech. 71 (1), 61–84.

Zhao, X.J., Bordas, S.P.A., Qu, J.M., 2013a. A hybrid smoothed extended finite element/level set method for modeling equilibrium shapes of nano-inhomogeneities. Comput. Mech. 52 (6), 1417–1428.

Zhao, X.J., Bordas, S.P.A., Qu, J.M., 2015. Equilibrium morphology of misfit particles in elastically stressed solids under chemo-mechanical equilibrium conditions. J. Mech. Phys. Solids 81, 1–21.

Zhao, X.J., Duddu, R., Bordas, S.P.A., Qu, J.M., 2013b. Effects of elastic strain energy and interfacial stress on the equilibrium morphology of misfit particles in heterogeneous solids. J. Mech. Phys. Solids 61 (6), 1433–1445.

Zhao, K., Pharr, M., Hartle, L., Vlassak, J.J., Suo, Z., 2012. Fracture and debonding in lithium-ion batteries with electrodes of hollow core–shell nanostructures. J. Power Sources 218, 6–14.